IEEE Access
Multidisciplinary | Rapid Review | Open Access Journal

Received 25 January 2024, accepted 14 February 2024, date of publication 20 February 2024, date of current version 29 February 2024.

Digital Object Identifier 10.1109/ACCESS.2024.3368397

RESEARCH ARTICLE

Near-Field Engineering in RIS-Aided Links: Beamfocusing Analytical Performance Assessment

SOTIRIS DROULIAS, GIORGOS STRATIDAKIS, (Graduate Student Member, IEEE), AND ANGELIKI ALEXIOU, (Member, IEEE)
Department of Digital Systems, University of Piraeus, 185 34 Piraeus, Greece

Corresponding author: Sotiris Droulias (sdroulias@unipi.gr)

This work was supported by the Horizon Europe Programme through the Smart Networks and Services Joint Undertaking project TERA6G (TERAhertz Integrated Systems Enabling 6G Terabit-Per-Second Ultra-Massive MIMO Wireless Networks) under Grant 101096949.

ABSTRACT Reconfigurable intelligent surfaces (RISs) are typically utilized in the far-field as an effective means of creating virtual line-of-sight (LOS) links to mediate non-LOS propagation in wireless communications via beamforming. Owing to their large surface and the multitude of scatterers, the use of RISs can be extended in the near-field, to transform the incident beam into a focused beam that is able to address the challenges of high frequencies more efficiently than conventional beamforming. In this paper we explain from a physics' standpoint how the RIS can engineer wavefronts to transform the incident beam into a focused beam targeted at the user, and we employ the angular spectrum representation approach to describe analytically the dynamics of beamfocusing. We derive analytical expressions that provide the necessary insight into the dependencies and trade-offs between crucial parameters, such as the incident beam's footprint on the RIS, the intended focal distance of the reflected beam, and the link topology. To assess the beamfocusing efficiency we provide metrics that are crucial for future applications, including energy efficient communications, wireless power transfer, tracking and localization.

INDEX TERMS Reconfigurable intelligent surface, beamfocusing, angular spectrum representation, near field.

I. INTRODUCTION

One of the most common functionalities of reconfigurable intelligent surfaces (RISs) regards redirecting an incident beam towards any desired direction, beyond specular reflection, essentially creating virtual line-of-sight (LOS) links to mediate non-LOS propagation. Owing to this unique feature, the RIS has been proposed as a means to bypass blockage, especially in high frequency communications, such as the terahertz (THz) band [1], [2], [3], [4], [5], [6], [7], [8], [9], [10]. As wireless communications are nowadays shifting to higher frequencies with the aim to meet the perpetual demand for increased bandwidth, it gradually becomes clear that, to achieve and maintain high quality of service, future networks are envisioned to be equipped with functionalities beyond conventional beamforming.

The associate editor coordinating the review of this manuscript and approving it for publication was Zaharias D. Zaharis.

A direct consequence of frequency upscale is that, for a certain aperture, a radiating element becomes electrically large, and the transition from the near- to the far-field moves to larger distances. Objects and users that at GHz frequencies were located in the far-field of the antennas, are now found within the near-field of large-scale antennas and RISs operating in the THz band, for example. The availability of electrically large surfaces opens up new opportunities for manipulating the wavefront of the radiated wave, to acquire curvature beyond the typical far-field planar form [11], [12], [13]. For example, by shaping the curvature of a beam into spherical wavefronts, beams that would typically diffract can now counteract spreading, and focus. While the RIS has been so far extensively studied within the context of beamforming, the possibility for beamfocusing has only recently been addressed [14], [15], [16], [17], [18], [19], [20], [21], [22], [23]. With beamfocusing, the incident power can be concentrated at controllable distances from the RIS, towards

© 2024 The Authors. This work is licensed under a Creative Commons Attribution 4.0 License.
For more information, see https://creativecommons.org/licenses/by/4.0/

any desired direction. Therefore, beamfocusing is ideal for dramatically increasing the received power in small areas, a key element for energy efficient communications [17], [24], [25], [26], [27] and localization applications [28], [29], [30], [31].

To exploit the full potential of beamfocusing, it is fundamental to understand the requirements for efficient and controllable formation of focal areas. The beamfocusing efficiency will depend on crucial parameters, such as the positioning of the RIS with respect to the transmitter and receiver, the properties of the beam footprint on the RIS, the reflection angle and the desired focal distance [32]. Therefore, there is a need for analytical models that can clarify the bounds imposed by the system design parameters on the link performance.

In this work, the RIS beamfocusing capabilities are studied in terms of the received power. The main contributions are summarized as follows.

- An exact analytical model for beamfocusing at oblique angles is derived. The model provides the spatial distribution of the focused beam and the power delivered to the user at any location.
- The derivation of the analytical model is based on explicit electromagnetic modeling, by means of the angular spectrum representation approach, which captures the full-wave propagation characteristics of the RIS-reflected beam, as predicted by Maxwell's equations.
- The analytical model provides insight into the interplay between crucial parameters, such as the positioning of the RIS with respect to the transmitter and receiver, and the properties of the beam footprint on the RIS.
- Metrics to assess the beamfocusing efficiency are introduced.
- The approach followed in this work provides simple guidelines for algorithm design and performance optimization.

II. SYSTEM MODEL

Let us consider a RIS located at the origin of the coordinate system shown in Fig. 1. A beam illuminates the RIS, and is subsequently reflected by the RIS towards a desired direction. The RIS reshapes the incident wavefront so that the reflected beam is focused at a desired focal distance. The directions of incidence and reflection are defined by the wavevectors $\mathbf{k}_i$ and $\mathbf{k}_r$, respectively, which are expressed with respect to the elevation (θ) and azimuth (φ) angles of incidence (subscript i) and reflection (subscript r), as shown in Fig. 1(a). In this work we consider beam steering on the $xz-$plane and, therefore, we may neglect the angle φ. The incident beam is generated by an access point (AP), the location of which is characterized by the distance d_{AP} from the RIS center and the angle $\theta_{\text{AP}} \equiv \theta_i$, as shown in Fig. 1(b). The location of the user equipment (UE) is characterized by the distance d_{UE} from the RIS center and the angle θ_{UE}. As shown in Fig. 1(c), the reflected beam may point towards any direction and, hence, to maximize the power delivery to the UE, it is necessary to bring the focal point at the UE location. This requires that the reflected beam is directed towards the UE, i.e. $\theta_r = \theta_{\text{UE}}$ and that the focal distance is equal to the RIS-UE distance, i.e. $f_0 = d_{\text{UE}}$.

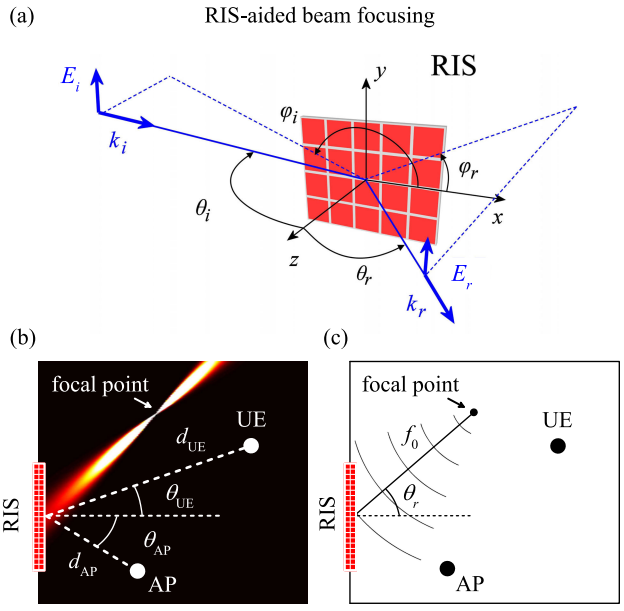

FIGURE 1. System model of a RIS-aided beamfocusing link. (a) The incident field, impinging along the direction characterized by the angles θ_i, φ_i, is focused along the direction characterized by the angles θ_r, φ_r (b) Cross-section of the focused beam on the $xz-$plane, illustrating the AP and UE locations relative to the RIS. (c) Schematic illustration of the spherical wavefronts of the focused beam that are directed at angle θ_r and converge at distance f_0. The power at the UE is maximized when $\theta_r = \theta_{\text{UE}}$ and $f_0 = d_{\text{UE}}$.

Given a certain AP-RIS-UE topology, we would like to know how the incident beam is redistributed by the RIS upon reflection, and what is the power delivered to the UE from the reflected beam, which is focused at a desired location. To this end, we need to calculate the field reflected from the RIS at any desired observation point (x, y, z). Here, we will follow the angular spectrum representation approach adopted in [18], according to which the reflected field can be calculated anywhere in the semi-infinite space $z > 0$, using only (a) the footprint of the incident field on the RIS and (b) the phase introduced by the RIS.

A. FOOTPRINT OF INCIDENT BEAM ON THE RIS

The footprint of the incident beam on the RIS depends on the properties of the AP antenna. For most practical cases the main lobe of the incident beam can be modeled by a Gaussian distribution [9], [18], [33], [34]. Without loss of generality we consider a $y-$polarized beam propagating on the $xz-$plane, the E-field of which at $z = 0$ is written as

$$\mathbf{E}_i(x, y) = E_0 \exp\left(-\frac{(x\cos\theta_i)^2 + y^2}{w_{\text{RIS}}^2}\right) \exp\left(-jk\sin\theta_i x\right)\hat{\mathbf{y}}, \quad (1)$$

where E_0 is a complex constant, w_{RIS} the radius of the footprint at normal incidence ($\theta_i = 0$), $k = 2\pi/\lambda$ is the free-space wavenumber and λ the wavelength. Note that this

model takes into account the fact that under oblique incidence ($\theta_i \neq 0$) the footprint acquires elliptical shape, with the major axis of the ellipse residing on the $x-$axis [33].

B. RIS REFLECTION COEFFICIENT

To perform beamfocusing it is necessary to transform the incident beam into spherical wavefronts that converge at the desired location, characterized by the focal distance f_0 and the angle θ_r, as schematically shown in Fig. 1(c). The role of the RIS is to introduce the necessary phase $\phi(x, y)$, in order to reshape the incident wavefront into the desired form, i.e. to add $\phi(x, y)$ to the phase of the incident wavefront. For polarization-preserving RIS, the footprint of the reflected beam on the RIS can be written as

$$\mathbf{E}_{\mathrm{RIS}}(x, y) = \Gamma(x, y)\mathbf{E}_i(x, y), \tag{2}$$

where $\Gamma(x, y) = |R| \exp(-j\phi(x, y))$ is the RIS reflection coefficient and $\mathbf{E}_i(x, y)$ the incident field at the RIS plane, i.e. the incident beam footprint. R is a complex constant that accounts for possible loss upon reflection ($|R| \leq 1$) and $\phi(x, y)$ is the phase introduced by the RIS.

For conventional beam steering, the RIS corrects the phase tilt of the incident wave, which has the form $\exp(-jk \sin\theta_i x)$ (see (1)), by adding a phase with the opposite slope and introduces a linear phase $\exp(-jk \sin\theta_r x)$, to form a wavefront that directs the wave towards the desired direction. Hence, for beam steering on the xz-plane, the RIS introduces the phase

$$\phi(x, y) = -k(\sin\theta_i - \sin\theta_r)x, \tag{3}$$

(for steering out of plane, see e.g. [9]).

For beamfocusing, after correcting the incident phase, the RIS must provide a phase of the form $\exp\left(-jk\sqrt{(f_0 \cos\theta_r)^2 + (x - f_0 \sin\theta_r)^2 + y^2}\right)$, and the phase introduced by the RIS is expressed as

$$\phi(x, y) = -k \sin\theta_i x + kf_0 \cos\theta_r \times \sqrt{1 + \left(\frac{x - f_0 \sin\theta_r}{f_0 \cos\theta_r}\right)^2 + \left(\frac{y}{f_0 \cos\theta_r}\right)^2}. \tag{4}$$

Note that, in the limit $f_0 \to \infty$, (4) approaches (3) (we may omit the global phase), i.e. corresponds to the phase for conventional beamsteering.

III. ANGULAR SPECTRUM REPRESENTATION APPROACH

Let us consider the field reflected from the RIS at any observation point (x, y, z), $\mathbf{E}_r(\mathbf{r}) = \mathbf{E}_r(x, y, z)$. In this notation, the reflected field right before departing from the RIS, i.e. on the xy-plane where the RIS surface resides, is $\mathbf{E}_r(x, y, 0) \equiv \mathbf{E}_{\mathrm{RIS}}(x, y)$. Its two-dimensional Fourier transform is

$$\hat{\mathbf{E}}_{\mathrm{RIS}}(k_x, k_y) = \frac{1}{4\pi^2} \iint_{-\infty}^{+\infty} \mathbf{E}_{\mathrm{RIS}}(x, y) e^{-j(k_x x + k_y y)} dx dy, \tag{5}$$

where x, y are the Cartesian transverse coordinates and k_x, k_y the corresponding spatial frequencies. Similarly, the inverse Fourier transform reads

$$\mathbf{E}_{\mathrm{RIS}}(x, y) = \iint_{-\infty}^{+\infty} \hat{\mathbf{E}}_{\mathrm{RIS}}(k_x, k_y) e^{j(k_x x + k_y y)} dk_x dk_y. \tag{6}$$

Note that the field $\mathbf{E}_{\mathrm{RIS}}$ and its Fourier transform $\hat{\mathbf{E}}_{\mathrm{RIS}}$ represent vectors and, hence, the Fourier integrals hold separately for each vector component. The field has to satisfy Maxwell's equations, which for free-space propagation reduce to the vector Helmholtz equation $(\nabla^2 + k^2)\mathbf{E}(\mathbf{r}) = 0$. Expressing similarly the reflected field $\mathbf{E}_r(x, y, z)$ via its Fourier transform and inserting it into the Helmholtz equation, we find that the Fourier spectrum $\hat{\mathbf{E}}_r$ of the reflected field evolves as

$$\hat{\mathbf{E}}_r(k_x, k_y; z) = \hat{\mathbf{E}}_{\mathrm{RIS}}(k_x, k_y) e^{jk_z z}, \tag{7}$$

where

$$k_z = \sqrt{k^2 - k_x^2 - k_y^2}. \tag{8}$$

After performing the inverse Fourier transform of (7) we find for arbitrary z

$$\mathbf{E}_r(x, y, z) = \iint_{-\infty}^{+\infty} \hat{\mathbf{E}}_{\mathrm{RIS}}(k_x, k_y) e^{j(k_x x + k_y y + k_z z)} dk_x dk_y, \tag{9}$$

which is known as the *angular spectrum representation* [35], [36]. The result of (9) states that the field at any $z > 0$ is determined entirely by its Fourier spectrum at $z = 0$. Hence, to calculate the reflected field, only knowledge of $\mathbf{E}_{\mathrm{RIS}}(x, y)$ is required, which is given by (2), using (1) and (4). Then, the reflected field at any observation point (x, y, z) is calculated using (5), the Fourier transform of $\mathbf{E}_{\mathrm{RIS}}(x, y)$, and inserting the result into (9). In (9), while the integration is performed in the entire $\mathbb{R}^2$ domain, components with imaginary k_z correspond to evanescent waves, which do not propagate. Therefore, we may reduce the domain of integration within the range $k_x^2 + k_y^2 < k^2$.

This technique provides the reflected power density distribution for any illumination conditions, from full to partial RIS illumination [33]. *Full illumination* refers to the case where the incident beam footprint extends beyond the size of the RIS. In this case the integration domain in (5) is limited within the area of the RIS. *Partial illumination* refers to the case where the incident beam footprint is smaller than the RIS [9], [18], [34]. Hence, we may neglect the RIS boundary and perform the integration of (5) in the entire $\mathbb{R}^2$ domain; the RIS size becomes effectively infinite. Importantly, in this case, we may simplify the integration of (9), to express the reflected power density in compact analytical form. For example, we can take advantage of the fact that the integrand in (9) contributes to the integration essentially at a narrow region around $k_r = k \sin\theta_r$, where the $k-$content of the reflected beam is distributed. Therefore, for plane waves or beams of finite extent that typically have a narrow $k-$content, we may expand k_z at the direction of

propagation of the reflected wave, i.e. around $k_x = k_r, k_y = 0$. This leads to the approximation of (8) (see Appendix A for details)

$$k_z \approx k\frac{3-\sec^2\theta_r}{2\cos\theta_r} + k_x\tan\theta_r^3 - \frac{k_x^2}{2k\cos^3\theta_r} - \frac{k_y^2}{2k\cos\theta_r}. \quad (10)$$

For $\theta_r = 0°$, this approximation reduces to the well-known parabolic form $k_z \approx k - (k_x^2 + k_y^2)/2k$ [18].

We may further simplify the analytical calculation of (9) by taking advantage of the relatively large curvature of ϕ in (4), required to focus the beam at distances larger than the RIS size. In this case we may expand (4) around the center of the RIS to obtain (see Appendix A for details)

$$\phi(x,y) \approx -k\sin\theta_i x + kf_0\left(1 - \frac{\tan^2\theta_r}{2}\right) + k\frac{(x\cos\theta_r - f_0\tan\theta_r)^2}{2f_0} + k\frac{y^2}{2f_0}. \quad (11)$$

For $\theta_r = 0°$, i.e. beam focusing along the z-axis, (11) reduces to the simple parabolic form $\phi(x,y) = -k\sin\theta_i x + kf_0 + k(x^2+y^2)/2f_0$ [18].

Using (1), (2) and (11) in (5) we calculate the k-spectrum of the reflected beam at the RIS plane, $\hat{\mathbf{E}}_{\text{RIS}}(k_x, k_y)$. The reflected field at any observation point on the $xz-$plane is calculated by inserting this result and (10) into (9), and the resulting power density $S_r = |E_r|^2/2Z_0$ is given by

$$S_r(x,z) = \frac{|E_0|^2}{2Z_0}|R|^2 \frac{1}{\sqrt{\left(1-\frac{z}{f_0\cos\theta_r}\right)^2 + \left(\frac{z}{z_R\cos\theta_r}\right)^2}} \times \frac{1}{\sqrt{\left(1-\frac{z}{f_0\cos\theta_r}\right)^2 + \left(\frac{z}{z_R\cos\theta_r}\right)^2\left(\frac{\cos\theta_i}{\cos\theta_r}\right)^4}} \times \exp\left[-\frac{2\,(x\cos\theta_r - z\sin\theta_r)^2}{w_{\text{RIS}}^2\left(\left(\frac{\cos\theta_r}{\cos\theta_i} - \frac{z}{f_0\cos\theta_i}\right)^2 + \left(\frac{z\cos\theta_i}{z_R\cos^2\theta_r}\right)^2\right)}\right], \quad (12)$$

where Z_0 is the free-space wave impedance and $z_R = \pi w_{\text{RIS}}^2/\lambda$ is the Rayleigh length. Note that, for $f_0 \to \infty$, (12) yields the received power for conventional beam forming [9], [18]. The choice $E_0 = \sqrt{4Z_0P_t\cos\theta_i/\pi w_{\text{RIS}}^2}$ ensures that $\iint |S_r|^2 = P_t|R|^2$, where P_t is the total power (Watts) of the incident beam.

Along the propagation direction of the focused beam, i.e. for $x = r\sin\theta_r, z = r\cos\theta_r$, the argument of the exponential term in (12) becomes zero, leading to a maximum power density expressed by the remaining prefactor

$$S_r(r) = \frac{2P_t\cos\theta_i}{\pi w_{\text{RIS}}^2}|R|^2 \frac{1}{\sqrt{\left(1-\frac{r}{f_0}\right)^2 + \left(\frac{r}{z_R}\right)^2}} \times \frac{1}{\sqrt{\left(1-\frac{r}{f_0}\right)^2 + \left(\frac{r}{z_R}\right)^2\left(\frac{\cos\theta_i}{\cos\theta_r}\right)^4}}. \quad (13)$$

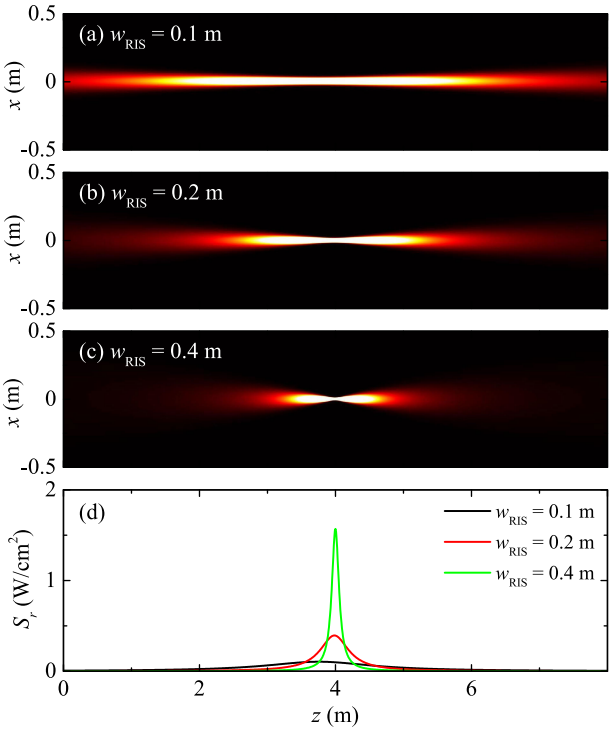

FIGURE 2. Impact of incident beam's footprint on the RIS, w_{RIS}, on beamfocusing. Cross-section of power density distribution on the $xz-$plane of a beam focused along the direction $\theta_r = 0°$ with $f_0 = 4$ m, and (a) $w_{\text{RIS}} = 0.1$ m, (b) $w_{\text{RIS}} = 0.2$ m, and (c) $w_{\text{RIS}} = 0.4$ m. (d) Power density along the beam center for the cases shown in panels (a)-(c).

By differentiating (13) with respect to r, the slope for $r \to 0$ acquires the positive value $4P_t|R|^2\cos\theta_i/\pi f_0 w_{\text{RIS}}^2$, while vanishes for $r \to \infty$. Therefore, there is always a maximum, which is expected at $r = f_0$. To understand how beamfocusing depends on the involved parameters, next we examine the derived expressions with examples of realistic scenarios.

IV. IMPACT OF RIS FOOTPRINT AND FOCAL DISTANCE ON RECEIVED POWER

Let us consider a D-band indoor scenario with operation frequency of 150 GHz. The AP is equipped with a directional antenna of tunable gain that transmits a beam of constant power $P_t = 1$ W towards the RIS. Depending on the position and orientation of the AP relative to the RIS, footprints of different size and ellipticity are captured by the RIS, all with the same total power. The RIS is lossless ($R = 1$) and focuses the incident beam towards $\theta_r = 0°$. In Fig. 2 we use (12) to examine beamfocusing as a function of the beam footprint, for intended focusing at $f_0 = 4$ m focal distance. For relatively small footprint ($w_{\text{RIS}} = 0.1$ m) we observe inefficient focusing, i.e. the power density is maximized sooner than f_0, with maximum that is relatively weak. However, with increasing footprint ($w_{\text{RIS}} = 0.2$ m, 0.4 m), the maximum power density improves dramatically and the focal point f_0 is quickly approached.

In Fig. 3 we examine the same scenario as a function of the focal distance, for constant footprint $w_{\text{RIS}} = 0.2$ m. The

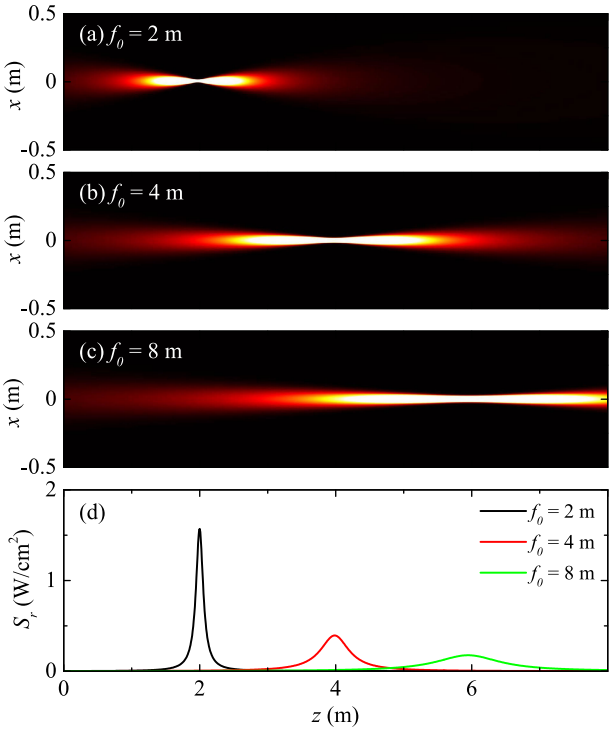

FIGURE 3. Impact of focal distance f_0 on beamfocusing. Cross-section of power density distribution on the $xz-$plane of a beam focused along the direction $\theta_r = 0°$ with $w_{RIS} = 0.2$ m, and (a) $f_0 = 2$ m, (b) $f_0 = 4$ m, and (c) $f_0 = 8$ m. (d) Power density along the beam center for the cases shown in panels (a)-(c).

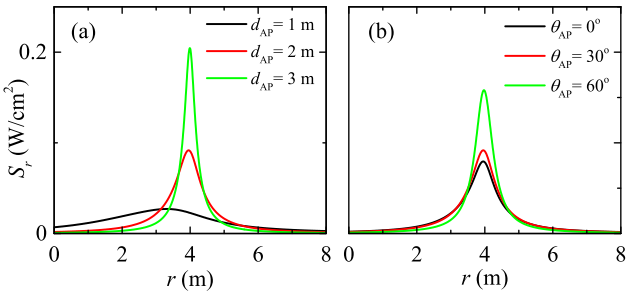

FIGURE 4. Impact of AP distance and orientation with respect to the RIS, on beamfocusing. Power density along the beam center, for AP locations characterized by (a) $\theta_{AP} = 30°$ and $d_{AP} = 1, 2, 3$ m (b) $d_{AP} = 2$ m and $\theta_{AP} = 0°, 30°, 60°$. In all examples the AP beam is focused by the RIS towards the focal point characterized by $\theta_r = 60°$ and $f_0 = 4$ m.

relatively large footprint enables efficient beamfocusing at the desired distance and the maximum power density reduces with increasing f_0.

To understand the observations in these two examples, let us examine the power density at the focal distance. By setting $r = f_0$ in (13) we obtain

$$S_r(r = f_0) = 2\pi \frac{P_t |R|^2}{\lambda^2} \frac{w_{\text{RIS}}^2}{f_0^2} \frac{\cos^2 \theta_r}{\cos \theta_i}. \tag{14}$$

The form of (14) implies that, for constant incident power P_t, the power density at a certain observation distance r is expected to increase with larger footprints (and/or angles of incidence), while it is expected to decrease with larger focal distances (and/or angles of reflection), in accord with our observations. The two general examples of Fig. 2 and Fig. 3 aim to provide insight into the underlying mechanisms of beamfocusing, beyond a specific AP-RIS-UE topology. Next, we examine explicitly the impact of the topology on beamfocusing.

A. IMPACT OF AP POSITION ON RECEIVED POWER

To understand how beamfocusing depends on the distance and orientation of the AP relative to the RIS, let us now consider a mobile AP with antenna of 30 dB constant gain.

In Fig. 4(a) the AP moves along the direction $\theta_{\text{AP}} = 30°$ and the RIS focuses the incident beam at $f_0 = 4$ m focal distance towards the direction $\theta_r = 60°$. Due to oblique incidence ($\theta_{\text{AP}} \neq 0$), the incident footprint has shape that is elliptical (see (1)), and size that increases with increasing distance d_{AP}. For $d_{\text{AP}} = 1, 2, 3$ m, the radius of the footprint becomes $w_{\text{RIS}} = 9, 18, 27$ cm, respectively (see Appendix B for details). Therefore, although the incident power is constant ($P_t = 1$ W), the maximum power density at the focal point increases with increasing AP-RIS distance.

In Fig. 4(b) the AP moves along a circular trajectory at constant distance $d_{\text{AP}} = 2$ m from the RIS, creating a footprint with $w_{\text{RIS}} = 18$ cm. As the AP departs from the RIS normal, the incident footprint becomes more elliptical, in turn increasing in size, and improving the maximum power density at the focal area, as shown in the examples for $\theta_{\text{AP}} = 0°, 30°, 60°$.

B. IMPACT OF FOCAL DISTANCE ON RECEIVED POWER

The power density at the UE can be calculated using (12) at the UE location, i.e. for $x = d_{\text{UE}} \sin \theta_{\text{UE}}$, $z = d_{\text{UE}} \cos \theta_{\text{UE}}$. To maximize the power at the UE we need to ensure that the focal point is located at the UE, i.e. that $\theta_r = \theta_{\text{UE}}$ and $f_0 = d_{\text{UE}}$. In this case, the focal point essentially follows the UE as it moves, guaranteeing that the maximum power is delivered. Solving in terms of d_{UE} we can retrieve the RIS-UE distance at which the power density acquires a desired threshold, S_{th}, that is

$$d_{\text{UE}}(\theta_{\text{UE}}) = z_R \sqrt{\frac{|R|^2}{S_{\text{th}}} \frac{2P_t \cos \theta_{\text{AP}}}{\pi w_{\text{RIS}}^2}} \frac{\cos \theta_{\text{UE}}}{\cos \theta_{\text{AP}}}. \tag{15}$$

The form of (15) implies that the trajectory of constant power forms a circle with radius $d_{\text{UE}}(0)/2$, centered at $(x = 0, z = d_{\text{UE}}(0)/2)$. As an example, in Fig. 5(a) we seek the UE positions at which the power density is constant and equal to $S_{\text{th}} = 0.4\,\text{W/cm}^2$, when the beam is focused at focal distance $f_0 = 4$ m. The UE positions that satisfy the imposed criterion are denoted by the white circle, which is expressed analytically by (15). The circle essentially marks the locus of constant power density delivered by several different focused beams. The examples marked with the letters A, B and C depict three such beams, and their power density evolution along each individual direction is shown in

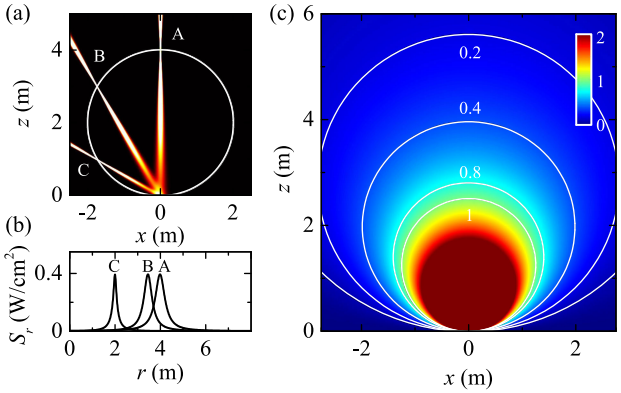

FIGURE 5. Beamfocusing at the UE position. (a) Spatial distribution of power density for the three example beams A, B, C, focusing along $\theta_r = 0°, 30°, 60°$, respectively. The white circle marks the locus of UE positions, where the received power is constant. (b) Cross-section along the propagation direction of beams A, B, C shown in (a). (c) Power density of beamfocusing at the UE position, as a function of the power density threshold S_{th}. The contour lines show examples of S_{th}, and represent the locus of UE positions, where the same received power can be achieved for each individual case.

Fig. 5(b). Requiring different threshold leads to a circle of different radius and the collection of all such possibilities is shown in Fig. 5(c) as a function of S_{th}.

V. BEAMFOCUSING EFFICIENCY ASSESSMENT

A. POWER ENHANCEMENT OF BEAMFOCUSING VS. BEAMFORMING

From the examples demonstrated so far, it is evident that beamfocusing offers the advantage of high power concentration at confined regions in space. This is particularly practical for increasing the power at the receiver, without the need for higher gain at the transmitter, e.g. for energy-efficient communications and power transfer applications [11]. To quantify the achievable enhancement in the received power we calculate the ratio of (13) over the received power in the absence of focusing ($f_0 \to \infty$), accounting for conventional steering. The enhancement factor, $e_f \equiv P_r/P_r(f_0 \to \infty)$, at $r = f_0$ yields

$$e_f = \sqrt{1+\left(\frac{z_R}{f_0}\right)^2}\sqrt{1+\left(\frac{z_R}{f_0}\right)^2\left(\frac{\cos\theta_i}{\cos\theta_r}\right)^4}. \tag{16}$$

In Fig. 6 we present (16), as a function of z_R/f_0 and $\cos\theta_i/\cos\theta_r$, which serves as a universal plot, capturing any combination of all the involved parameters. In our examples, where $z_R/f_0 > 12$ and $\cos\theta_i/\cos\theta_r > 0.5$, the minimum achievable enhancement is in the order of $e_f \sim 10^2$.

B. FWHM OF FOCAL AREA

The ability to control the size of the focal spot is crucial for partitioning the radial distance along the focusing direction, e.g. for localization applications [11], [20], [21]. Under the constraint of constant incident beam power, the size of the focal spot changes inversely with the beam maximum, which in turn depends on both the focusing direction and the focal distance, as captured by (14) and the examples studied so far.

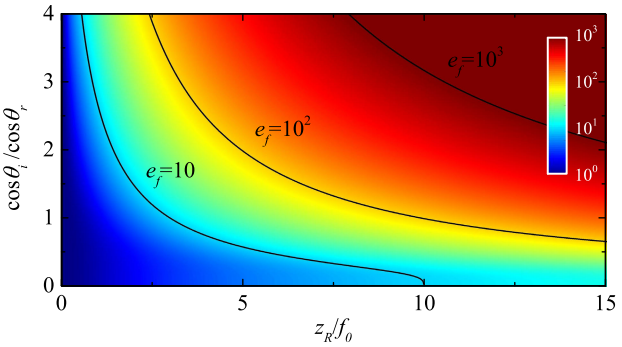

FIGURE 6. Enhancement factor, e_f, expressing the increase in the achievable power delivery to the UE due to beamfocusing, over the respective with beamforming.

The extent of the focal spot can be expressed by its Full Width Half Maximum (FWHM) along the propagation direction, w_{FWHM}, which for $\theta_i = \theta_r = 0°$ is given by (see Appendix C for derivation)

$$w_{\text{FWHM}} = \frac{2z_R}{1+\left(\frac{z_R}{f_0}\right)^2}. \tag{17}$$

The functional form of (17) dictates that w_{FWHM} increases with f_0 and reduces with w_{RIS}. As an example, in Fig. 7(a) we plot the trace of beam maximum (dashed black lines) and FWHM of focal spot (shaded areas) as a function of the steering angle θ_r, for $w_{\text{RIS}} = 0.25\,\text{m}$ and variable f_0. Indeed, as f_0 increases, the FWHM increases as well. Note, however, that according to (17) we can achieve a focal spot with constant FWHM, regardless of the focal distance, if we increase w_{RIS} with increasing f_0. For example, as demonstrated in Fig. 7(b), using (17) with $f_0 = 4\,\text{m}$ and $w_{\text{RIS}} = 0.25\,\text{m}$, we find that upon changing f_0 to 8 m and 2 m, we can achieve a constant FWHM if we choose w_{RIS} to be 0.5 m and 0.125 m, respectively. The constant ratio w_{RIS}/f_0 in this example is not accidental; note that, in the limit $z_R \gg f_0$, (17) takes the simple form

$$w_{\text{FWHM}} \xrightarrow{z_R \gg f_0} \frac{2f_0^2}{z_R} = \frac{4f_0^2}{kw_{\text{RIS}}^2}, \tag{18}$$

indicating that a proportional change in f_0 and w_{RIS} leads to the same FWHM. In our examples $z_R/f_0 > 12$, i.e. we are well within the asymptotic limit of (17), as can be verified in Fig. 7(c). The simple form of (18) provides a straightforward way to partition the radial distance in segments of equal size, essentially forming zones of constant width. The formation of such zones and, in particular, the ability to control their extent, is crucial for tracking and localization applications, where a sensing-based communication scheme is able to detect the UE distance within controllable resolution, and transmit data with high quality of service.

VI. MULTI-BEAM OPERATION

For multiple users that reside in the RIS near field, the RIS can split the incident beam into a multitude of focused beams,

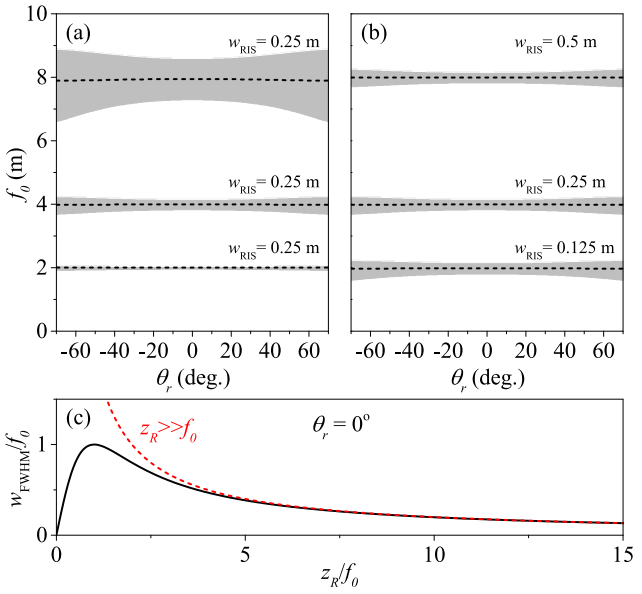

FIGURE 7. Properties of focal spot. (a) Trace of beam maximum (dashed black lines) and FWHM of focal spot (shaded areas) as a function of the steering angle θ_r for $w_{RIS} = 0.25$ m and variable f_0. (b) Same as in (a) with tunable w_{RIS}, in order to achieve the same FWHM for the different f_0's. (c) Plot of (17) and asymptotic limit for $z_R \gg f_0$.

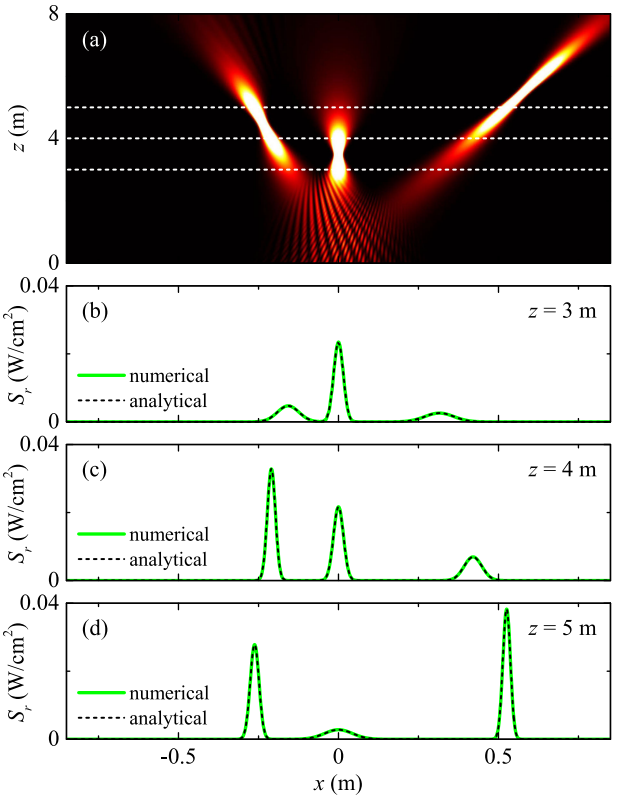

FIGURE 8. Multiple simultaneously focused beams, for broadcast to selected multiple users. (a) Power density of numerically propagated reflected field. The incident beam has footprint $w_{RIS} = 20$ cm and carries total power $P_t = 1$ W, which is split equally by the RIS into three beams, characterized by $\theta_r = -3°, 0°, 6°$, and $f_0 = 4.5$ m, 3.5 m, 5.5 m, respectively. The white dashed lines mark cross-sections of the beams at (b) $z = 3$ m, (c) $z = 4$ m, and (d) $z = 5$ m, where comparison with the analytical model of (12) for single beam is also shown.

to simultaneously serve all users. In this case, each reflected beam is associated with an individual reflection coefficient $\Gamma_n(x, y) = |R| \exp(-j\phi_n(x, y))$, accounting for the n^{th} user, with $\phi_n(x, y)$ given by (4) (or its approximation, (11)). The angle θ_r and the focal distance f_0 have distinct values for each n, $\theta_{r,n}$ and $f_{0,n}$, respectively, thus accommodating reflected beams, directed and focused towards each user. The footprint at the RIS is then written as the linear superposition

$$\mathbf{E}_{\text{RIS}}(x, y) = \frac{1}{\sqrt{N}} \sum_{n=1}^{N} \Gamma_n(x, y)\mathbf{E}_i(x, y), \tag{19}$$

which is a generalization of (2) to N beams. The $1/\sqrt{N}$ prefactor is chosen to ensure that the incident power is preserved and equally distributed between the reflected beams, which are assumed to be spatially separated so that they interfere weakly (see Appendix D for details). Using (19) to integrate (9) leads to the analytical expression for multiple focused beams. Note that, because the total footprint is a linear superposition of N individual contributions, the total reflected field can be calculated in a straightforward manner, by solving for the n^{th} E-field, $\mathbf{E}_{r,n}$, and expressing the total field as $\mathbf{E}_{r,\text{total}} = \sum_{n=1}^{N} \mathbf{E}_{r,n}$. The total power density, which is $\sim |\mathbf{E}_{r,\text{total}}|^2$, will eventually be cast in a rather long and unpractical analytical form; yet, we can take advantage of the fact that, for spatially separated beams that do not interfere significantly with each other, $|\mathbf{E}_{r,\text{total}}|^2 \approx \sum_{n=1}^{N} |\mathbf{E}_{r,n}|^2$. In this case, we can apply the expressions derived in our work, which describe the dynamics of a single beam, to each of the simultaneously generated focused beams, individually.

As an example, in Fig. 8 we examine $N = 3$ simultaneously generated focused beams, and we compare the full numerical propagation of the beams using (9), with the analytical expression (12), applied to each of the three beams, individually. The incident beam has total power $P_t = 1$ W and footprint radius $w_{\text{RIS}} = 20$ cm, and is split into three beams of equal power upon reflection. The beams are reflected towards the directions characterized by the angles $\theta_{r,1} = -3°, \theta_{r,2} = 0°$ and $\theta_{r,3} = 6°$, and the focal lengths $f_{0,1} = 4.5$ m, $f_{0,2} = 3.5$ m and $f_{0,3} = 5.5$ m, respectively. In Fig. 8(a) we present the numerical solution of (9), as a function of the propagation distance z, using (19). The dashed lines denote cross-sections at distance $z = 3$ m, 4 m and 5 m, which are shown in panels (b),(c) and (d), respectively. Together with the numerical cross-sections (green solid lines) is also shown the analytically calculated power density (black dashed lines), using (12) with $\Gamma = \Gamma_n$, separately applied for $n = 1, 2, 3$. Note how, despite the beam interference that dominates close to the RIS, the analytical expression successfully reproduces the numerically calculated beam profile, especially at distances where the beams evolve into distinct, spatially separated beams. These observations enable us to use our analytical results to any number of simultaneously generated focused

beams that are spatially separated, thus keeping the simplicity of our analytical expressions and the associated metrics, and generalizing the analysis and conclusions to multiple focused beams. Importantly, we can go beyond conventional beamfocusing, where an incident wave is focused into a single focal area, to design beams directed towards multiple directions with multiple focal points, for broadcast to selected multiple users.

Our framework can be applied to general multi-user scenarios, in conjuction with a multiple access scheme. For example, in a Time Division Multiple Access (TDMA) scheme, the RIS focuses the incident beam towards different directions and distances at different time slots, to successively serve each user. Similarly, in a Space Division Multiple Access (SDMA) scheme, different areas of the RIS are devoted to simultaneously focus multiple beams towards multiple users. In environments with severe multipath, where the instantaneous focused power may change due to fading, our framework can be directly extended to model beams with statistical properties (see e.g. [34]).

VII. CONCLUSION

As wireless communications are nowadays shifting to higher operation frequencies, taking advantage of the near-field offered by electrically large RISs opens up new opportunities for manipulating the wavefront of beams, to enrich communications with functionalities beyond conventional beamforming. In this work, we studied near-field engineering in RIS-aided links, in which the RIS transforms the incident beam into a focused beam, and we assessed the RIS beamfocusing capabilities analytically, using explicit electromagnetic modeling. To describe beamfocusing with a physically consistent model, the derivations were based on the angular spectrum representation approach, which captures the dynamics of free-space wave propagation in compliance with Maxwell's equations. With our model, we demonstrated the dependencies and trade-offs between crucial parameters, such as the incident beam's footprint on the RIS, the intended focal distance of the reflected beam, and the link topology. To assess the beamfocusing efficiency we provided metrics that are crucial for future applications, such as energy efficient communications, tracking and localization, and we demonstrated the theoretically expected performance with examples of typical D-band indoor scenarios.

APPENDIX A
VALIDITY OF APPROXIMATIONS

To calculate (10) we expand (8) around the direction of propagation, which is characterized by $k_x = k_r, k_y = 0$, where $k_r = k\sin\theta_r$. First, expansion around $k_y = 0$ leads to

$$k_z \sim \sqrt{k^2 - k_x^2} - \frac{k_y^2}{2\sqrt{k^2 - k_x^2}}, \tag{20}$$

where we have retained all terms up to 2^{nd} order. Next, expansion of (20) around $k_x = k_r$ leads to

$$k_z \sim \sqrt{k^2 - k_r^2} - \frac{k_r(k_x - k_r)}{\sqrt{k^2 - k_r^2}} - \frac{k^2(k_x - k_r)^2}{2(k^2 - k_r^2)^{\frac{3}{2}}} - \frac{k_y^2}{2\sqrt{k^2 - k_r^2}}, \tag{21}$$

where we have retained all terms up to 2^{nd} order. Substitution of $k_r = k\sin\theta_r$ in (21) leads to the result of (10).

To calculate (11) we expand (4) around the center of the RIS, i.e. at $x = 0, y = 0$. Keeping all terms up to 2^{nd} order leads to the result of (11).

To verify the validity of the approximations (10) and (11) we have compared the analytically derived (12) with exhaustive full-wave numerical propagation examples under extreme conditions, e.g. at large angles of incidence and reflection. In this section we demonstrate the validity of the approximations (10) and (11) through comparison with their respective full form. In the following examples the AP is located in front of the RIS ($\theta_{\mathrm{AP}} = 0°$), creating a footprint of $w_{\mathrm{RIS}} = 0.15\,\mathrm{m}$ on the RIS. The RIS focuses the incident beam along three different directions characterized by $\theta_r = 0°, 30°, 60°$.

In Fig. 9(a) we plot (10) for $\theta_r = 0°$, which approximates the parabolic form of (8) in a relatively large region around $k_x = k_y = 0$, where the k-content of the reflected beam is located. This is illustrated in Fig. 9(b), where we show a cross-section of (10) along $k_y/k_0 = 0$ (red dashed line) as well as the full form of k_z for comparison (solid black line). The gray region marks the cross-section of the beam's k-content, verifying that within its extent, where integration takes place, (8) and (10) coincide. In the remaining panels we present the respective plots for $\theta_r = 30°$ (Fig. 9(c),(d)) and $\theta_r = 60°$ (Fig. 9(e),(f)). Note that the footprint used in these examples is relatively narrow and leads to a relatively wide k-content. For larger footprint, the beam k-content is narrower, and the error in (10) is further suppressed.

In Fig. 10(a) we plot (11), the approximation of (4), which for $\theta_r = 0°$ has a parabolic form centered at $x = y = 0$. Using the full form of ϕ, in Fig. 10(b) we plot the relative phase error, which we define as $(\phi - \phi_{\mathrm{approx.}})/\phi$, where ϕ accounts for (4) and $\phi_{\mathrm{approx.}}$ for (11). The solid circle marks the FWHM of the incident beam. In the remaining panels we present the respective plots for $\theta_r = 30°$ (Fig. 10(c),(d)) and $\theta_r = 60°$ (Fig. 10(e),(f)). Note how the center of the parabolic phase moves along the x-axis with increasing θ_r. In all cases the relative error is practically below 0.1%.

APPENDIX B
DERIVATION OF FOOTPRINT RADIUS IN TERMS OF THE ANTENNA GAIN

The footprint of the AP beam on the RIS can be expressed using (1) with $E_0 = \sqrt{4Z_0P_t\cos\theta_i/\pi w_{\mathrm{RIS}}^2}$, as

$$S_{\mathrm{RIS}} = \frac{2P_t\cos\theta_i}{\pi w_{\mathrm{RIS}}^2}U_t, \tag{22}$$

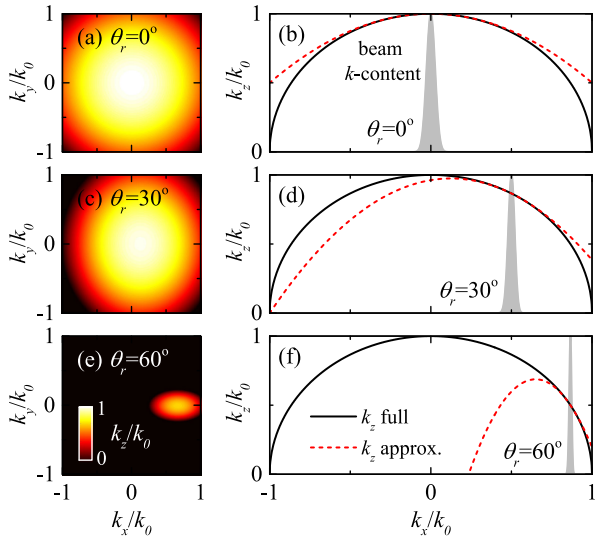

FIGURE 9. k_z approximation for a RIS that focuses the incident beam at $f_0 = 4$ m distance. (a),(b) $\theta_r = 0°$, (c),(d) $\theta_r = 30°$, and (e),(f) $\theta_r = 60°$. (a),(c),(e) k_z approximation given by (10). (b),(d),(f) Cross-section at $k_y/k_0 = 0$ of (10) (dashed red line) and its full form (8) (solid black line). The gray region depicts the $k-$content of the reflected beam of $w_{\text{RIS}} = 0.15$ m.

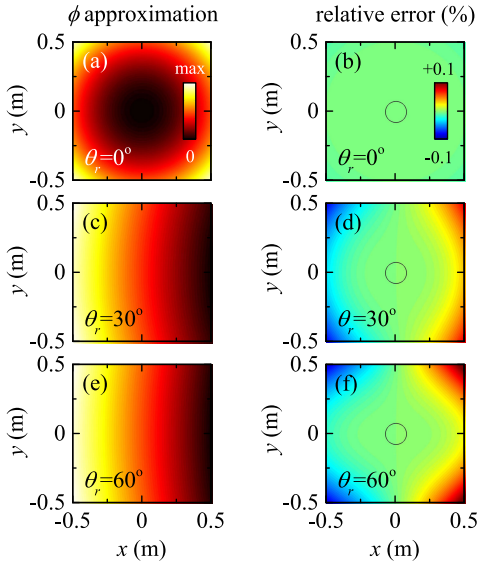

FIGURE 10. ϕ approximation for the RIS of Fig. 9. (a),(b) $\theta_r = 0°$, (c),(d) $\theta_r = 30°$, and (e),(f) $\theta_r = 60°$. (a),(c),(e) ϕ approximation given by (11). (b),(d),(f) Relative error of (11). The solid circle marks the FWHM of the incident beam.

with

$$U_t = \exp\left(-\frac{(x\cos\theta_i)^2 + y^2}{w_{\text{RIS}}^2}\right)^2, \tag{23}$$

expressing the AP radiation pattern at distance d_{AP}, where the RIS is located. The power density of (22) can be alternatively expressed in terms of G_t, the AP gain, as:

$$S_{\text{RIS}} = G_{tU_t}\frac{P_t\cos\theta_i}{4\pi d^2}, \tag{24}$$

where d is the radius of the sphere centered at the AP. For pencil beams $d \sim d_{\text{AP}}$ and, upon simple inspection of (22) and (24), we reach the final result

$$G_t = 8\left(\frac{d_{\text{AP}}}{w_{\text{RIS}}}\right)^2. \tag{25}$$

APPENDIX C
DERIVATION OF FWHM OF FOCAL AREA

To determine the FWHM of the focal spot we need to find the distance at which the power density is maximized. For $\theta_i = \theta_r = 0°$, differentiation of (13) with respect to the propagation distance r yields the focal distance

$$r_{focal} = \frac{f_0}{1 + \left(\frac{f_0}{z_R}\right)^2}, \tag{26}$$

at which the power density is maximized and becomes equal to

$$S_r(r = r_{focal}) = \frac{2P_t\cos\theta_i}{\pi w_{\text{RIS}}^2}|R|^2\left[1 + \left(\frac{z_R}{f_0}\right)^2\right]. \tag{27}$$

Using (27) to solve (13) for $S_r = S_r(r = r_{focal})/2$ in terms of w_{RIS}, yields two solutions $w_{\text{RIS}\pm}$

$$w_{\text{RIS}\pm} = \frac{\pm z_R + \frac{z_R^2}{f0}}{1 + \left(\frac{z_R}{f_0}\right)^2}, \tag{28}$$

corresponding to the two edges of the focal spot along r, where the threshold criterion is fulfilled. The FWHM of the focal spot along r is then $w_{\text{FWHM}} = w_{\text{RIS}+} - w_{\text{RIS}-}$.

APPENDIX D
RIS REFLECTION COEFFICIENT FOR MULTI-BEAM OPERATION

The total reflected field can be expressed as the linear superposition of the field of the individual beams, $\mathbf{E}_{r,\text{total}} = \sum_{n=1}^{N}\mathbf{E}_{r,n}$. At $z = 0$ the total field $\mathbf{E}_{r,\text{total}}$ becomes simply the footprint $\mathbf{E}_{\text{RIS}}$, and the individual fields are expressed in terms of the incident field as $\mathbf{E}_{r,n} = w_n\Gamma_n\mathbf{E}_i$, where Γ_n is the reflection coefficient for the n^{th} beam with $w_n \in \mathbb{R}$ accounting for the weight with which the n^{th} beam is reflected. Hence, the footprint takes the form

$$\mathbf{E}_{\text{RIS}} = \sum_{n=1}^{N} w_n\Gamma_n\mathbf{E}_i. \tag{29}$$

For a lossless RIS, the power of the reflected beam must be equal to that of the incident, i.e.

$$\iint\frac{|\mathbf{E}_{\text{RIS}}|^2}{2Z_0}dxdy = \iint\frac{|\mathbf{E}_i|^2}{2Z_0}dxdy, \tag{30}$$

where $|\mathbf{E}_{\text{RIS}}|^2 = |\sum_{n=1}^{N} w_n\Gamma_n|^2|\mathbf{E}_i|^2$. For beams that are spatially separated we may simplify $|\mathbf{E}_{r,\text{total}}|^2 \approx$

$\sum_{n=1}^{N} |\mathbf{E}_{r,n}|^2$, which leads to $|\mathbf{E}_{\text{RIS}}|^2 \approx \sum_{n=1}^{N} |w_n \Gamma_n|^2 |\mathbf{E}_i|^2$. Note that $\sum_{n=1}^{N} |w_n \Gamma_n|^2 = \sum_{n=1}^{N} w_n^2 |R|^2 = \sum_{n=1}^{N} w_n^2$ ($|R| = 1$ for lossless RIS) and, hence, (30) leads to $\sum_{n=1}^{N} w_n^2 = 1$. For equally distributed power among the reflected beams $w_1 = w_2 = \ldots w_N$, which leads to $w_n = 1/\sqrt{N}$.

REFERENCES

[1] Q. Wu and R. Zhang, "Beamforming optimization for wireless network aided by intelligent reflecting surface with discrete phase shifts," *IEEE Trans. Commun.*, vol. 68, no. 3, pp. 1838–1851, Mar. 2020.

[2] L. Dai, B. Wang, M. Wang, X. Yang, J. Tan, S. Bi, S. Xu, F. Yang, Z. Chen, M. D. Renzo, C.-B. Chae, and L. Hanzo, "Reconfigurable intelligent surface-based wireless communications: Antenna design, prototyping, and experimental results," *IEEE Access*, vol. 8, pp. 45913–45923, 2020.

[3] E. N. Papasotiriou, A. A. Boulogeorgos, A. Stratakou, and A. Alexiou, "Performance evaluation of reconfigurable intelligent surface assisted D-band wireless communication," in *Proc. IEEE 3rd 5G World Forum (5GWF)*, Sep. 2020, pp. 360–365.

[4] X. Qian, M. Di Renzo, J. Liu, A. Kammoun, and M.-S. Alouini, "Beamforming through reconfigurable intelligent surfaces in single-user MIMO systems: SNR distribution and scaling laws in the presence of channel fading and phase noise," *IEEE Wireless Commun. Lett.*, vol. 10, no. 1, pp. 77–81, Jan. 2021.

[5] W. Tang, M. Z. Chen, X. Chen, J. Y. Dai, Y. Han, M. Di Renzo, Y. Zeng, S. Jin, Q. Cheng, and T. J. Cui, "Wireless communications with reconfigurable intelligent surface: Path loss modeling and experimental measurement," *IEEE Trans. Wireless Commun.*, vol. 20, no. 1, pp. 421–439, Jan. 2021.

[6] C. Pan, H. Ren, K. Wang, J. F. Kolb, M. Elkashlan, M. Chen, M. Di Renzo, Y. Hao, J. Wang, A. L. Swindlehurst, X. You, and L. Hanzo, "Reconfigurable intelligent surfaces for 6G systems: Principles, applications, and research directions," *IEEE Commun. Mag.*, vol. 59, no. 6, pp. 14–20, Jun. 2021.

[7] Q. Wu, S. Zhang, B. Zheng, C. You, and R. Zhang, "Intelligent reflecting surface-aided wireless communications: A tutorial," *IEEE Trans. Commun.*, vol. 69, no. 5, pp. 3313–3351, May 2021.

[8] I. Yildirim, A. Uyrus, and E. Basar, "Modeling and analysis of reconfigurable intelligent surfaces for indoor and outdoor applications in future wireless networks," *IEEE Trans. Commun.*, vol. 69, no. 2, pp. 1290–1301, Feb. 2021.

[9] G. Stratidakis, S. Droulias, and A. Alexiou, "Analytical performance assessment of beamforming efficiency in reconfigurable intelligent surface-aided links," *IEEE Access*, vol. 9, pp. 115922–115931, 2021.

[10] M. Khalily, O. Yurduseven, T. J. Cui, Y. Hao, and G. V. Eleftheriades, "Engineered electromagnetic metasurfaces in wireless communications: Applications, research frontiers and future directions," *IEEE Commun. Mag.*, vol. 60, no. 10, pp. 88–94, Oct. 2022.

[11] G. Stratidakis, S. Droulias, and A. Alexiou, "Perceptive, resilient, and efficient networks assisted by reconfigurable intelligent surfaces," 2023, *arXiv:2312.01009*.

[12] A. Singh, V. Petrov, H. Guerboukha, I. V. A. K. Reddy, E. W. Knightly, D. M. Mittleman, and J. M. Jornet, "Wavefront engineering: Realizing efficient terahertz band communications in 6G and beyond," 2023, *arXiv:2305.12636*.

[13] K. Zhi, C. Pan, H. Ren, K. K. Chai, C.-X. Wang, R. Schober, and X. You, "Performance analysis and low-complexity design for XL-MIMO with near-field spatial non-stationarities," 2023, *arXiv:2304.00172*.

[14] O. Yurduseven, S. D. Assimonis, and M. Matthaiou, "Intelligent reflecting surfaces with spatial modulation: An electromagnetic perspective," *IEEE Open J. Commun. Soc.*, vol. 1, pp. 1256–1266, 2020.

[15] H. Zhang, N. Shlezinger, F. Guidi, D. Dardari, M. F. Imani, and Y. C. Eldar, "Beam focusing for multi-user MIMO communications with dynamic metasurface antennas," in *Proc. IEEE Int. Conf. Acoust., Speech Signal Process. (ICASSP)*, Jun. 2021, pp. 4780–4784.

[16] H. Zhang, N. Shlezinger, F. Guidi, D. Dardari, M. F. Imani, and Y. C. Eldar, "Beam focusing for near-field multiuser MIMO communications," *IEEE Trans. Wireless Commun.*, vol. 21, no. 9, pp. 7476–7490, Sep. 2022.

[17] N. M. Tran, M. M. Amri, J. H. Park, D. I. Kim, and K. W. Choi, "Reconfigurable-intelligent-surface-aided wireless power transfer systems: Analysis and implementation," *IEEE Internet Things J.*, vol. 9, no. 21, pp. 21338–21356, Nov. 2022.

[18] S. Droulias and A. Alexiou, "Reconfigurable intelligent surface: An angular spectrum representation approach," in *Proc. 56th Asilomar Conf. Signals, Syst., Comput.*, Oct. 2022, pp. 413–418.

[19] M. Salah, M. M. Elsherbini, and O. A. Omer, "RIS-focus: On the optimal placement of the focal plane for outdoor beam routing," *IEEE Access*, vol. 10, pp. 53053–53065, 2022.

[20] M. Cui, Z. Wu, Y. Lu, X. Wei, and L. Dai, "Near-field MIMO communications for 6G: Fundamentals, challenges, potentials, and future directions," *IEEE Commun. Mag.*, vol. 61, no. 1, pp. 40–46, Jan. 2023.

[21] Z. Wu and L. Dai, "Multiple access for near-field communications: SDMA or LDMA?" *IEEE J. Sel. Areas Commun.*, vol. 41, no. 6, pp. 1918–1935, Jun. 2023.

[22] J. An, C. Yuen, L. Dai, M. Di Renzo, M. Debbah, and L. Hanzo, "Toward beamfocusing-aided near-field communications: Research advances, potential, and challenges," 2023, *arXiv:2309.09242*.

[23] A. Kosasih and E. Björnson, "Finite beam depth analysis for large arrays," 2023, *arXiv:2306.12367*.

[24] C. Huang, A. Zappone, G. C. Alexandropoulos, M. Debbah, and C. Yuen, "Reconfigurable intelligent surfaces for energy efficiency in wireless communication," *IEEE Trans. Wireless Commun.*, vol. 18, no. 8, pp. 4157–4170, Aug. 2019.

[25] M. Ahsan, S. Jamil, M. T. Ejaz, and M. S. Abbas, "Energy efficiency maximization in RIS-assisted wireless networks," in *Proc. Int. Conf. Comput., Electron. Electr. Eng. (ICE Cube)*, Oct. 2021, pp. 1–6.

[26] Z. Yang, M. Chen, W. Saad, W. Xu, M. Shikh-Bahaei, H. V. Poor, and S. Cui, "Energy-efficient wireless communications with distributed reconfigurable intelligent surfaces," *IEEE Trans. Wireless Commun.*, vol. 21, no. 1, pp. 665–679, Jan. 2022.

[27] Z. Li, J. Zhang, J. Zhu, and L. Dai, "RIS energy efficiency optimization with practical power models," in *Proc. Int. Wireless Commun. Mobile Comput. (IWCMC)*, Jun. 2023, pp. 1172–1177.

[28] H. Wymeersch, J. He, B. Denis, A. Clemente, and M. Juntti, "Radio localization and mapping with reconfigurable intelligent surfaces: Challenges, opportunities, and research directions," *IEEE Veh. Technol. Mag.*, vol. 15, no. 4, pp. 52–61, Dec. 2020.

[29] J. He, F. Jiang, K. Keykhosravi, J. Kokkoniemi, H. Wymeersch, and M. Juntti, "Beyond 5G RIS mmWave systems: Where communication and localization meet," *IEEE Access*, vol. 10, pp. 68075–68084, 2022.

[30] H. Zhang, B. Di, K. Bian, Z. Han, H. V. Poor, and L. Song, "Toward ubiquitous sensing and localization with reconfigurable intelligent surfaces," *Proc. IEEE*, vol. 110, no. 9, pp. 1401–1422, Sep. 2022.

[31] T. Ma, Y. Xiao, X. Lei, L. Zhang, Y. Niu, and G. K. Karagiannidis, "Reconfigurable intelligent surface assisted localization: Technologies, challenges, and the road ahead," *IEEE Open J. Commun. Soc.*, vol. 4, pp. 1430–1451, 2023.

[32] G. Stratidakis, S. Droulias, and A. Alexiou, "Beam-forming and beam-focusing capabilities in RIS-aided communications," in *IEEE Future Networks World Forum*. Baltimore, MD, USA: Imagining the Network of the Future, Symposium on Terahertz Communications for Future Networks, Nov. 2023, pp. 13–15.

[33] G. Stratidakis, S. Droulias, and A. Alexiou, "Understanding the RIS efficiency: From partial to full illumination," in *Proc. IEEE 23rd Int. Workshop Signal Process. Adv. Wireless Commun. (SPAWC)*, Jul. 2022, pp. 1–5.

[34] E. N. Papasotiriou, S. Droulias, and A. Alexiou, "Analytical characterization of RIS-aided terahertz links in the presence of beam misalignment," *IEEE J. Sel. Topics Signal Process.*, vol. 17, no. 4, pp. 850–860, Jun. 2023.

[35] M. Born, E. Wolf, A. B. Bhatia, P. C. Clemmow, D. Gabor, A. R. Stokes, A. M. Taylor, P. A. Wayman, and W. L. Wilcock, *Principles of Optics: Electromagnetic Theory of Propagation, Interference and Diffraction of Light*, 7th ed. Cambridge, U.K.: Cambridge Univ. Press, 1999.

[36] L. Novotny and B. Hecht, *Principles of Nano-Optics*, 2nd ed. Cambridge, U.K.: Cambridge Univ. Press, 2012.

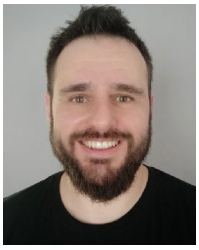

SOTIRIS DROULIAS received the Diploma degree in electrical and computer engineering and the Ph.D. degree in nonlinear photonics from the National Technical University of Athens, Athens, Greece, in 2001 and 2007, respectively. From 2009 to 2012, he was an Adjunct Lecturer with the University of Patras, Patras, Greece, and from 2012 to 2020, he was a member of the Photonic-, Phononic- and Meta-Materials Group, FORTH-IESL, Crete, Greece. He is currently a Research Associate with the Department of Digital Systems, ICT School, University of Piraeus, Piraeus, Greece. He has worked on several EC-funded projects. He is the author of more than 50 papers and two book chapters. His research interests include metamaterials, photonic crystals, metasurfaces, nanolasers, plasmonics, and active media. In 2019, he was a recipient of the Best Poster Award for his work on metasurface lasers in META 2019, Lisbon, Portugal. In 2020, he was recognized as an Outstanding Reviewer by the Institute of Physics (IOP) and serves as a reviewer for international scientific journals. He has received several talk invitations at prestigious conferences.

GIORGOS STRATIDAKIS (Graduate Student Member, IEEE) was born in Athens, Greece, in 1990. He received the bachelor's degree in telecommunications engineering from the Department of Telecommunications Science and Technology, University of Peloponnese, in 2016, and the master's degree in digital communications and networks from the Department of Digital Systems, University of Piraeus, in 2018, where he is currently pursuing the Ph.D. degree in wireless communications. In 2017, he joined the Department of Digital Systems, University of Piraeus, where he conducts research in the area of wireless communications.

ANGELIKI ALEXIOU (Member, IEEE) received the Diploma degree in electrical and computer engineering from the National Technical University of Athens, in 1994, and the Ph.D. degree in electrical engineering from the Imperial College of Science, Technology and Medicine, University of London, in 2000. Since May 2009, she has been a Faculty Member with the Department of Digital Systems, where she conducts research and teaches bachelor's and master's courses in broadband communications and advanced wireless technologies. Prior to this appointment, she was with Bell Laboratories, Wireless Research, and Lucent Technologies, (later Alcatel-Lucent, now NOKIA), Swindon, U.K., first as a member of technical staff (from January 1999 to February 2006) and later as the Technical Manager (from March 2006 to April 2009). She is currently a Professor with the Department of Digital Systems, ICT School, University of Piraeus, Greece. She is also a Project Coordinator of the H2020 TERRANOVA Project (ict-terranova.eu) and the Technical Manager of the H2020 ARIADNE Project (ict-ariadne.eu). Her current research interests include radio interface for systems beyond 5G, MIMO, THz wireless technologies, reconfigurable intelligent surfaces, efficient resource management for ultra-dense wireless networks, machine-to-machine communications and artificial intelligence, and machine learning for future wireless systems. She is a member of the Technical Chamber of Greece. She was a co-recipient of the Bell Labs President's Gold Award for contributions to the Bell Labs Layered Space-Time (BLAST) Project, in 2002, and the Central Bell Labs Teamwork Award for role model teamwork and technical achievements in the IST FITNESS Project, in 2004. She is the Chair of the Working Group on Radio Communication Technologies and High Frequencies Radio Technologies of the Wireless World Research Forum.